

Probing Pulsar Winds Using Inverse Compton Scattering

Lewis Ball^a and J. G. Kirk^b

^a *Research Centre for Theoretical Astrophysics, University of Sydney, N.S.W. 2006, Australia*

^b *Max-Planck-Institut für Kernphysik, Postfach 10 39 80, D-69029, Heidelberg, Germany*

Abstract

We investigate the effects of inverse Compton scattering by electrons and positrons in the unshocked winds of rotationally-powered binary pulsars. This process can scatter low energy target photons to produce gamma rays with energies from MeV to TeV. The binary radio pulsars PSR B1259–63 and PSR J0045–73 are both in close eccentric orbits around bright main sequence stars which provide a huge density of low energy target photons. The inverse Compton scattering process transfers momentum from the pulsar wind to the scattered photons, and therefore provides a drag which tends to decelerate the pulsar wind. We present detailed calculations of the dynamics of a pulsar wind which is undergoing inverse Compton scattering, showing that the deceleration of the wind of PSR B1259–63 due to ‘inverse Compton drag’ is small, but that this process may confine the wind of PSR J0045–73 before it attains pressure balance with the outflow of its companion star. We calculate the spectra and light curves of the resulting inverse Compton emission from PSR B1259–63 and show that if the size of the pulsar wind nebula is comparable to the binary separation, then the γ -ray emission from the unshocked wind may be detectable by atmospheric Cerenkov detectors or by the new generation of satellite-borne γ -ray detectors such as INTEGRAL and GLAST. This mechanism may therefore provide a direct probe of the freely-expanding regions of pulsar winds, previously thought to be invisible.

Keywords: Pulsars; Inverse Compton scattering; gamma-rays; Cerenkov telescopes; Pulsars: individual (PSR B1259–63, PSR J0045–73)

PACS: 95.30Jx; 95.55Ka; 97.60Gb; 98.70Rz

Rotationally-powered pulsars are rapidly rotating neutron stars whose rotation is slowing at a readily measurable rate. It is generally accepted that the rotational energy is carried away by a wind of electrons, positrons, and possibly ions. Models for the best studied rotationally-powered pulsar – the Crab – suggest that the wind expansion is highly relativistic with a bulk Lorentz factor of $\gamma_w \sim 10^6$ [Rees & Gunn 1974]. A number of authors have investigated the inverse Compton scattering of emission from the neutron star itself by the electrons and positrons of the pulsar wind both close to the surface [Zhang, Qiao & Han 1997; Qiao & Lin 1998; Luo & Protheroe 1998] and at about the distance of the light-cylinder [Bogovalov & Aharonian 1999; Aharonian & Bogovalov 1999]. At much larger radii, pulsar winds may be confined by pressure balance with the surrounding medium, as in the Crab nebula, in which case the electrons and positrons in the wind will be accelerated and isotropised at the shock which terminates the relativistic wind. The inverse Compton emission by electrons and positrons in the shocked pulsar wind has been considered, addressing both the scattering of self-produced synchrotron photons [De Jager & Harding 1992], of diffuse background target photons [for a review see Harding 1996], and of photons from a binary companion [Kirk, Ball & Skjæraasen 1999]. However, until recently, it has generally been thought that the intermediate region between the light cylinder and the termination shock could not be observed directly.

In this paper we investigate inverse Compton scattering by the electrons and positrons in this unshocked region of pulsar winds. Chernyakova & Illarionov [1999] have also considered aspects of this problem, such as the deceleration of the pulsar wind when the scatterings can be treated in the Thomson limit, and the spectrum of scattered photons when the wind deceleration and absorption by photon-photon pair production could be neglected. Here we present a more detailed treatment, including deceleration in the Thomson and Klein-Nishina regimes and the effects of absorption. We apply our formalism to two binary pulsar systems in which there is a huge density of target photons from a luminous companion star and show that the pulsar PSR B1259–63 should produce detectable gamma-ray emission from the scattering of the companion star photons by the unshocked pulsar wind, provided it is not confined to a small region around the pulsar. The strong dependence of the target photon density on the position with respect to the star, coupled with the fact that the target photons may be assumed to all be propagating radially from the star, and so are unidirectional at each point where a scattering occurs, implies that the scattered emission will have a strong dependence on orbital phase. In close binary systems the scattering process can have a significant influence on the dynamics of the unshocked wind, and may provide the first direct probe of the freely-expanding region of a pulsar wind.

PSR B1259–63 is the only known galactic radio pulsar which is orbiting a main-sequence companion. It is in a close, highly eccentric orbit ($e \sim 0.87$)

around SS2883, a B2e star of radius $R_* \sim 6R_\odot$ and luminosity $L_* \sim 8.8 \times 10^3 L_\odot$ [Johnston et al. 1992, 1994, 1996]. The system is thought to be 1.5 kpc from the Earth and at periastron the pulsar is only $23R_* \approx 10^{11}$ m from its companion. The only other similar binary pulsar system, PSR J0045–73 [Kaspi et al. 1994a,b; Bell et al. 1995], is in the Small Magellanic Cloud, and is the most distant pulsar known. It is in an orbit of eccentricity 0.81 around an even more luminous companion, a B1 V star of radius $6.4R_\odot$ and luminosity $1.2 \times 10^4 L_\odot$, and at periastron the pulsar is just $26R_\odot \approx 2 \times 10^{10}$ m from its companion.

The spin-down luminosity of PSR B1259–63 is significant, $L_p = 8.3 \times 10^{28}$ W, and it is likely that this drives a relatively strong wind. The wind is most probably confined by pressure balance with the strong outflow from the pulsar’s Be-star companion [Melatos, Johnston & Melrose 1995], in which case the pulsar wind slows to a subsonic outflow at a termination shock. The already relativistic electrons and positrons from the pulsar wind are isotropised and accelerated to even higher energies at this shock. The unpulsed X-rays observed throughout the binary orbit of this system [Hirayama et al. 1996] are thought to result from synchrotron emission from electrons and positrons in the shocked region of the pulsar wind [Tavani & Arons 1997]. Kirk et al. [1999] have shown that inverse Compton scattering of photons from the Be star, by the electrons and positrons of the shocked pulsar wind, is likely to produce a flux of hard γ -rays that would be detectable by atmospheric Cerenkov telescopes.

If just 10^{-3} of the spin down luminosity of PSR B1259–63 is converted into γ -rays by inverse Compton scattering in the *unshocked* wind, the resulting flux would be detectable at energies somewhere in the MeV–TeV range depending on the Lorentz factor of the pulsar wind. The lower spin down luminosity and greater distance to PSR J0045–73 means that it should be unobservable in hard γ -rays. Nevertheless the binary separation of this system is even smaller than that of PSR B1259–63 and the companion star is also more luminous, so inverse Compton scattering by the unshocked wind may affect the dynamics of this system.

In the following sections we present equations describing the deceleration of the pulsar wind by ‘inverse Compton drag’ – the energy losses of the unshocked electrons and positrons due to inverse Compton scattering of the companion-star photons, and the intensity and spectrum of the energetic scattered photons. We show that the inverse Compton losses cannot contain the wind of PSR B1259–63 before it attains the radius at which pressure balance with the Be-star outflow occurs. These losses may significantly decelerate the wind of PSR J0045–73 at times near periastron within a range of angles about the line joining the pulsar and its companion. We present examples of the emitted inverse-Compton spectrum and of the light curves from PSR B1259–63,

showing that the emission from the unshocked wind should be detectable as gamma-rays. The signal from the unshocked wind is quite different from that from the shocked wind, so that if a variable gamma-ray signal is detected from this system, these two possible source mechanisms should be readily distinguishable.

1 Dynamics of the pulsar wind

We assume that a relativistic, radially directed wind containing electrons, positrons and an admixture of ions emerges from the pulsar. This wind propagates in an ambient radiation field and the particles in the wind interact incoherently with the ambient photons. The most important interaction is Compton scattering by the electrons and positrons. In this section we outline the essential steps in the derivation of the equations for the dynamics of a pulsar wind subject to inverse Compton scattering. Further details are presented in Appendix A.

Observations and models of the wind of the Crab pulsar suggest that it emerges nearly tangentially at around the light cylinder radius and that the Poynting flux dominates the outflow at such radii [Rees & Gunn 1974]. However, by the time the wind interacts with the surrounding nebula the importance of the magnetic field is greatly diminished and the outgoing flux is dominated by the particle momentum. Models suggest that the wind ultimately attains a bulk Lorentz factor of order $\gamma_w = 10^6$ [Kennel & Coroniti 1984; Emmering & Chevalier 1987]. While this picture is well accepted, the physics responsible for the transformation of the wind is poorly understood. Nevertheless, it is likely that the wind evolves relatively rapidly into a cold, relativistic, particle dominated, radial outflow. We will assume that at the radii of interest here, which are well beyond the light cylinder, the electrons and positrons of the pulsar wind may be taken to be monoenergetic, with Lorentz factor equal to that of the bulk flow, γ_w .

We denote by $n_\gamma(\epsilon, \mathbf{R}, \vec{\Omega}) d\vec{\Omega} d\epsilon$ the differential number density of target photons moving within the solid angle $d\vec{\Omega}$ of the unit vector $\vec{\Omega}$ at position \mathbf{R} with respect to the star, with energy between $E = \epsilon m_e c^2$ and $(\epsilon + d\epsilon)m_e c^2$. We investigate the deceleration of the wind in the highly anisotropic radiation field comprising the light from a companion star which is treated as a point source. The target photons are treated as monochromatic.

An individual electron of Lorentz factor γ scatters target photons at an average rate

$$\dot{N}_{\text{ic}} = c \int d\vec{\Omega} \int d\epsilon_{\text{in}} \frac{\epsilon'_{\text{in}}}{\gamma\epsilon_{\text{in}}} n_{\gamma}(\epsilon_{\text{in}}, \mathbf{R}, \vec{\Omega}) \sigma_{\text{KN}}(\epsilon'_{\text{in}}) \quad (1)$$

[Jones 1965], where $\sigma_{\text{KN}}(x)$ is the Klein-Nishina cross section. (Note that when used alone the term ‘electron’ may be taken to refer to both electrons and positrons in the pulsar wind.) Unprimed quantities are measured in the observer’s frame and primed quantities are measured in the rest frame of the incoming electron. Energies are expressed in units of $m_e c^2$ so that $E_{\text{in}} = \epsilon_{\text{in}} m_e c^2$ is the energy of the target photon in the observer’s frame, $E'_{\text{in}} = \epsilon'_{\text{in}} m_e c^2$ the energy of the target photon seen in the electron rest frame. The process of triplet pair production, $e\gamma \rightarrow 3e$, can be ignored since the maximum value of $\gamma\epsilon_{\text{in}}$ which we consider is of the order 100 [Mastichiadis 1991].

The average rate of change of energy of the photon field is given by an integral similar to that in Eq. (1), but weighted by the factor $\epsilon_{\text{out}} - \epsilon_{\text{in}}$, where $E_{\text{out}} = \epsilon_{\text{out}} m_e c^2$ is the energy of the scattered photon given by

$$\epsilon_{\text{out}} = \frac{\epsilon'_{\text{in}} \gamma (1 - \beta \cos \theta'_{\text{out}})}{1 + \epsilon'_{\text{in}} (1 - \cos \theta'_{\text{sc}})} \quad (2)$$

with θ'_{out} the angle between the outgoing photon and the velocity vector of the observer’s frame and θ'_{sc} the scattering angle, both measured in the electron rest frame. The rate of change of radial momentum is calculated in a similar fashion, using $-\epsilon_{\text{out}} \cos \theta_{\text{out}} + \epsilon_{\text{in}} \cos \theta_{\text{in}}$ as the weighting function, with θ_{in} and θ_{out} the angles between the incoming and outgoing photons and the vector opposite the incoming electron velocity in the observer’s frame.

As a result of Compton scattering the electrons and positrons of the pulsar wind lose both energy and radial momentum, but gain a small amount of transverse momentum, so that the gas is both decelerated and heated. In the case of an ultra-relativistic wind the heating is small and may be neglected (see Appendix A). The deceleration of the wind due to inverse Compton drag is then given by the equation

$$\frac{d\gamma_{\text{w}}}{dr} = -\frac{3\eta\sigma_{\text{T}}}{8\beta_{\text{w}}} \int d\vec{\Omega} d\epsilon_{\text{in}} \frac{\epsilon'_{\text{in}}{}^2}{\epsilon_{\text{in}}} \left(1 - \frac{\epsilon_{\text{in}}}{\gamma\epsilon'_{\text{in}}} - \frac{\epsilon_{\text{in}}}{\gamma}\right) n_{\gamma}(\epsilon_{\text{in}}, \mathbf{R}, \vec{\Omega}) F_{\text{loss}}(\epsilon'_{\text{in}}) \quad (3)$$

in which $\beta_{\text{w}} = (1 - \gamma_{\text{w}}^{-2})^{1/2}$, σ_{T} is the Thompson cross section, and F_{loss} is a function defined by Jones [1965]

$$F_{\text{loss}}(x) = \frac{-2x(10x^4 - 51x^3 - 93x^2 - 51x - 9)}{3x^4(1 + 2x)^3} + \frac{(x^2 - 2x - 3) \ln(2x + 1)}{x^4} \quad (4)$$

[see also Kirk et al. 1999]. The parameter η is the fraction of the wind luminosity carried by electrons and positrons:

$$\eta = \frac{1}{1 + Mn_i/(m_e n_e)} \quad (5)$$

with M the ion mass and m_e the electron mass, and n_i and n_e the ion and electron number densities at any given radius.

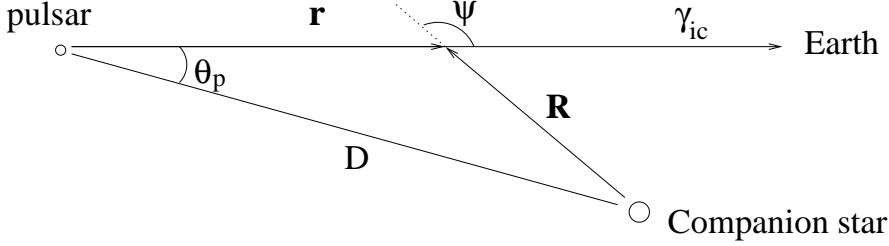


Fig. 1. Sketch of the binary system defining angles and distances used in the text. When the target photons originate from a companion star, the target field can be written in the form

$$n_\gamma(\epsilon_{in}, \mathbf{R}, \vec{\Omega}) = N(R)\delta(\epsilon_{in} - \epsilon_0)\delta(\vec{\Omega} - \hat{\mathbf{R}}) \quad (6)$$

where $N(R) = L_*/(4\pi R^2 ch\nu_0)$ is the photon density, $\epsilon_0 = h\nu_0/m_e c^2$ is the dimensionless energy of the companion star photons, $\hat{\mathbf{R}} = \mathbf{R}/R$ is a unit vector, and L_* is the stellar luminosity. We denote the binary separation of the pulsar and its companion star by D , and introduce the dimensionless distance $\hat{r} = r/D$. Inserting Eq. (6) into (3), making the approximation $\beta_w \approx 1$, we find

$$\frac{d\gamma_w}{d\hat{r}} \approx -\frac{3\eta N_0 \sigma_T D}{8 \sin^2 \theta_p} \frac{\epsilon'_{in}{}^2 \sin^2 \psi}{\epsilon_0} \left(1 - \frac{\epsilon_0}{\gamma_w \epsilon'_{in}} - \frac{\epsilon_0}{\gamma_w}\right) F_{\text{loss}}(\epsilon'_{in}) \quad (7)$$

where $N_0 = N(D)$, $\epsilon'_{in} = \gamma_w \epsilon_0 (1 - \beta_w \cos \psi)$ and ψ is the angle between the vectors \mathbf{R} and \mathbf{r} . The geometry is shown in Fig. 1. Note that the angle ψ is a function of position \hat{r} :

$$\cos \psi = \frac{\hat{r} - \cos \theta_p}{\sqrt{1 + \hat{r}^2 - 2\hat{r} \cos \theta_p}}. \quad (8)$$

Equation (7) implies that $\dot{\gamma}_w > 0$ when $\epsilon'_{in} < \epsilon_0/(\gamma_w - \epsilon_0)$ meaning that the target photons actually accelerate electrons traveling almost directly away from the companion star for which $\cos \psi \approx 1$. The condition for this to occur is

$$\cos \psi > \frac{1}{\sqrt{1 - 1/\gamma_w^2}} \left(1 - \frac{1}{\gamma_w(\gamma_w - \epsilon_0)}\right); \quad (9)$$

for $\gamma_w = 10^6$ and $\epsilon_0 = 10^{-5}$ this is equivalent to $|\psi| \lesssim 10^{-6}$, which is satisfied only when the electrons are moving essentially radially away from the companion star.

2 An approximate treatment

Before applying the results of §1 and deriving the spectrum of the scattered radiation, we consider a greatly simplified treatment obtained by approximating the scattering cross-section by the Thompson cross-section and assuming that the energy distribution of the scattered photons is a delta function. In this approximation an electron of Lorentz factor γ emits monochromatic photons of energy $\epsilon_{\text{out}} = 4\gamma^2\epsilon_{\text{in}}/3$ and the reaction rate is simply $N\sigma_T c$. The equation governing the deceleration of the wind is then

$$\frac{d\gamma_w}{dr} \approx -\frac{4}{3}\eta\gamma_w^2\epsilon_{\text{in}}N\sigma_T. \quad (10)$$

If the density of target photons remains roughly constant on the length scale upon which the wind is decelerated, it follows that

$$r_{\text{decel}} \approx [\eta\gamma_w(0)\epsilon_{\text{in}}N\sigma_T]^{-1} \quad (11)$$

$$= 7.8 \times 10^9 \left(\frac{10^6}{\eta\gamma_w(0)} \right) \left(\frac{10^{12} \text{eV cm}^{-3}}{U_{\text{rad}}} \right) \text{ meters}, \quad (12)$$

where the scaling of the energy density of the target photons has been chosen to be close to that of PSR B1259–63 at periastron.

We next define a dimensionless spectral energy distribution $\mathcal{F}(r)$, which describes how the radiation builds up along the line of sight within the pulsar wind. At the outer boundary $r = r_{\text{max}}$ of the source, the final, observable value is attained: $\mathcal{F}(r_{\text{max}}) = EF_E 4\pi d^2 / L_w$ where F_E is the energy flux density at the Earth of photons of energy E , and d is the distance to the pulsar. The equation for the generation of the spectral energy density is then

$$\frac{d\mathcal{F}}{dr} = \frac{\eta}{\gamma_w(0)} N\sigma_T \epsilon_{\text{out}}^2 \delta(\epsilon_{\text{out}} - 4\gamma_w^2\epsilon_{\text{in}}/3). \quad (13)$$

Under the same assumption that the density of target photons is roughly constant over the distance r_{decel} , the emitted spectral energy distribution is

$$\mathcal{F} = \frac{1}{2} \sqrt{\frac{\epsilon_{\text{out}}}{\epsilon_{\text{out}}^+}} \quad (14)$$

extending from a maximum at $\epsilon_{\text{out}} = \epsilon_{\text{out}}^+ = 4\gamma_w^2(0)\epsilon_{\text{in}}/3$ down to a minimum which is a function of the physical extent of the wind.

The approximations given by Eqs. (12) and (14) can be applied to PSR B1259–63 and PSR J0045–73 at periastron using the appropriate physical parameters which are summarized in Table 1. The energy density in the target radiation field near the surface of PSR B1259–63 at the time of periastron is roughly $6 \times 10^{11} \text{ eV cm}^{-3}$, which implies $r_{\text{decel}} \approx 1.3 \times 10^{10} \text{ m} \sim 0.1 D_{\tau}$, where $D_{\tau} = 9.6 \times 10^{10} \text{ m}$ is the separation of the stars at periastron. Taken at face value this estimate suggests that the inverse Compton drag may be so efficient as to decelerate the pulsar wind completely before it attains the radius at which it would otherwise reach pressure balance with the Be star outflow. Furthermore this estimate implies that there should be a substantial energy flux at the Earth ($\sim 10^3 \text{ eV cm}^{-2} \text{ s}^{-1}$) concentrated in TeV photons. This corresponds to a photon flux of $\sim 10^{-9} \text{ cm}^{-2} \text{ s}^{-1}$, roughly 10^3 times higher than the sensitivity threshold of the imaging Cerenkov detector operated by the CANGAROO collaboration, and clearly conflicts with the marginal detection found by that experiment [Sako et al. 1997].

For PSR J0045–73 the energy density in the target radiation field at periastron is even higher, $U_{\text{rad}} \sim 2 \times 10^{13} \text{ eV cm}^{-3}$, whence $r_{\text{decel}} \approx 1.3 \times 10^{10} \text{ m} \sim 0.02 D_{\tau}$ with $D_{\tau} = 1.8 \times 10^{10} \text{ m}$ for this system. However, the much greater distance of this source makes it uninteresting for gamma-ray observations.

These simple estimates indicate that inverse Compton drag on the unshocked winds of these binary pulsars may be important. However the Klein-Nishina corrections to the scattering cross section are significant in these systems, as are the effects of the changing angle ψ and the changing density of target photons encountered by the scattering electrons as they propagate radially from the pulsar. We include these effects in the next sections.

Table 1

Parameters for the PSR B1259–63 and PSR J0045–73 systems. References are: 1–Johnston et al. [1996]; 2–Johnston et al. [1994]; 3–Underhill & Doazan [1982]; 4–Kaspi et al. [1994a]; 5–Kaspi et al. [1994b]; 6–Bell et al. [1995].

Parameter	PSR B1259–63		PSR J0045–73		
	Value	Ref.	Value	Ref.	
Pulsar					
period	P	47.762 ms	1	0.926 s	4
period derivative	\dot{P}	2.279×10^{-15}	1	4.486×10^{-15}	5
surface magnetic field	B_p	3.3×10^7 T	1	2.1×10^8 T	4
spin down luminosity	L_p	8.3×10^{28} W	1	2.2×10^{25} W	
Companion star					
spectral type		B2	2	B1 V	6
effective temperature	T_{eff}	2.28×10^4 K	3	2.4×10^4 K	6
radius	R_*	$6.0R_\odot$ (4.2×10^9 m)	3	$6.4R_\odot$ (4.5×10^9 m)	6
luminosity	L_*	$8.8 \times 10^3 L_\odot$ (3.3×10^{30} W)	3	$1.2 \times 10^4 L_\odot$ (4.6×10^{30} W)	6
effective photon energy	$\epsilon_0 = 2.7k_B T_{\text{eff}}/(mc^2)$	10^{-5}		10^{-5}	
mass	M_*	$10M_\odot$ (2×10^{31} kg)	3	$8.8M_\odot$ (1.8×10^{31} kg)	6
System					
eccentricity	e	0.87	1	0.81	4
periastron separation	D_τ	$23R_*$ (9.6×10^{10} m)		$4R_*$ (1.8×10^{10} m)	
apastron separation	D_a	$331R_*$ (1.4×10^{12} m)		$38R_*$ (1.7×10^{11} m)	
orbital inclination	i	35°	1	44°	6
distance	d	1.5 kpc	1	57.5 kpc	4

3 Inverse Compton emission from the unshocked wind

The basic approximation made in computing the inverse Compton emission of a relativistic particle is that the scattered photons are emitted in the direction of motion of the particle. Thus in the case of scattering by a radial pulsar wind, an observer sees photons produced at all points along the radius vector from the pulsar to the point at which the wind is either decelerated by radiation drag, or shocked, or simply runs out of target photons. In addition, scattered photons of sufficiently high energy may be absorbed by pair production on the same population of target photons via the process $\gamma\gamma \rightarrow e^+e^-$. The probability for pair production, like the scattering rate, is a function of position along the radius vector. In this section we derive expressions for the inverse Compton emission from the unshocked wind, including the effects of pair-production absorption. Further details are presented in Appendix B.

Observations of the Crab nebula suggest that in that case at least, the pulsar wind has an energy-dependent anisotropy [Aschenbach & Brinkmann 1975; Hester et al. 1995]. However, for simplicity we assume that the pulsar wind is independent of latitude and longitude. The distribution function of monoenergetic, radially directed electrons in the wind may then be written as

$$n_e(\gamma, \mathbf{r}, \vec{\Omega}) = N_e(r) \delta[\gamma - \gamma_w(r)] \delta(\vec{\Omega} - \hat{\mathbf{r}}), \quad (15)$$

where $N_e(r) = \eta L_w / [4\pi r^2 c \beta_w \gamma_w(0) m_e c^2]$, and L_w is the luminosity of the pulsar wind, which is taken to be equal to the spin-down luminosity. It is relatively straightforward to incorporate a more complicated model, provided the flow remains radial.

The specific intensity of radiation $I(\epsilon_{\text{out}}, r)$ is governed by the radiative transport equation

$$\frac{dI}{dr} = \left(\frac{L_w}{4\pi}\right) \frac{\eta \epsilon_{\text{out}}}{\gamma_w(0) m_e c^3} \frac{dN_\gamma}{d\epsilon_{\text{out}} dt} + I \frac{d\tau}{dr}, \quad (16)$$

where $dN_\gamma/d\epsilon_{\text{out}} dt$ is the differential rate of emission of inverse Compton scattered photons by a single electron, and τ is the optical depth between the observer and the point r due to pair production. Since r is measured from the pulsar outwards, it follows that $d\tau/dr \leq 0$. More details are presented in Appendix B.

When the target radiation originates from a companion star, as specified in Eq. (6), the photon production rate can be written as

$$\frac{dN_\gamma}{dt d\epsilon_{\text{out}}} = N(R) \sigma_{\text{TC}} c \mathcal{H}(\epsilon_{\text{out}}, \cos \psi), \quad (17)$$

where $\mathcal{H}(\epsilon_{\text{out}}, \cos \psi)$ is related to the quantity $dN_\gamma/dtd\epsilon_{\text{out}}[d\epsilon_{\text{in}}dx']$ derived by Ho & Epstein [1989] and is defined in Appendix B.

In terms of the dimensionless radius $\hat{r} = r/D$, the dimensionless spectral energy distribution $\mathcal{F}(r)$ introduced in the previous section ($\mathcal{F}(\infty) = 4\pi d^2 E F_E / L_w$ where F_E is the flux and d the distance to the object) builds up in the pulsar wind according to:

$$\frac{d\mathcal{F}}{d\hat{r}} = \left(\frac{\eta N_0 \sigma_T D}{\gamma_w(0) \sin^2 \theta_p} \right) \epsilon_{\text{out}}^2 \mathcal{H}(\epsilon_{\text{out}}, \cos \psi) \sin^2 \psi + \frac{d\tau}{d\hat{r}} \mathcal{F}, \quad (18)$$

where θ_p is the angle between the line joining the stars and the line of sight. The absorption optical depth obeys the equation [Kirk et al. 1999]

$$\frac{d\tau}{d\hat{r}} = - \left(\frac{N_0 \sigma_T D}{\sin^2 \theta_p} \right) \sin^2 \psi (1 - \cos \psi) \hat{\sigma}_{\gamma\gamma}(\bar{\epsilon}), \quad (19)$$

where $\hat{\sigma}_{\gamma\gamma}(z)$ is the cross section for pair production in units of σ_T (see Appendix B), which is to be evaluated with argument $\bar{\epsilon} = \sqrt{\epsilon_{\text{out}} \epsilon_0 (1 - \cos \psi) / 2}$.

The computation of the inverse Compton luminosity of the pulsar wind in the radiation field of its companion star therefore reduces to the integration of equations (7) and (18), with the optical depth gradient given by (19).

4 Inverse Compton drag on the winds of PSR B1259–63 & PSR J0045–73

Equation (7) can be numerically integrated to obtain the Lorentz factor of the radial wind as a function of r . Figure 2 shows the results for four different values of θ_p , for parameters appropriate to PSR B1259–63 and PSR J0045–73 as given in Table 1, assuming that the wind momentum is carried entirely by electrons and positrons, i.e. $\eta = 1$. When $\theta_p = 0$ the electrons are traveling straight towards the companion star and inverse Compton drag is at its most effective because the collisions are head on and the density of target photons increases as $(1 - \hat{r})^{-2}$. For large values of θ_p the drag is relatively ineffective because the electron–photon collisions are far from head on, and furthermore, the target photon density drops as the electrons propagate away from the companion star.

The curves for $\theta_p = 0$ shown in Fig. 2 can be compared to the simple estimates presented in §2. Figure 2a shows that in the head-on case, inverse Compton drag stops electrons in the wind of PSR B1259–63 at $\hat{r} \approx 0.9$ compare to the simple estimate $r_{\text{decel}} \sim 0.1D_\tau$. On the other hand, Fig. 2b shows that head-on

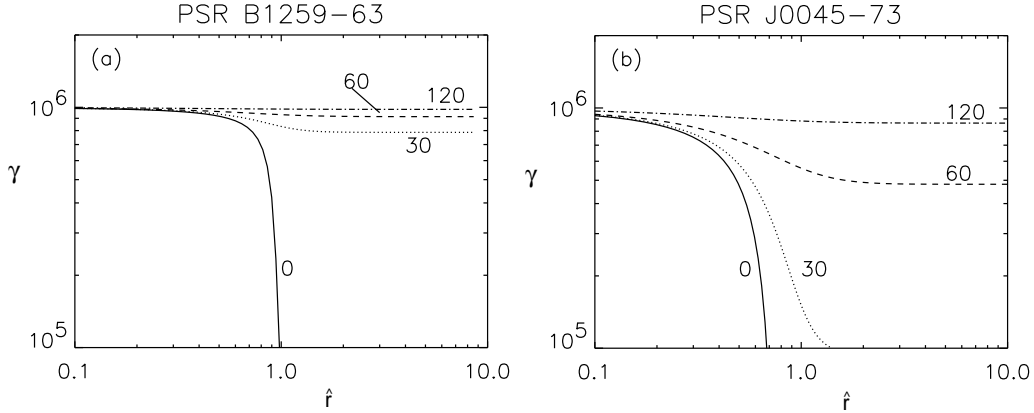


Fig. 2. Lorentz factor $\gamma_w(\hat{r})$ of a radial wind with $\gamma_w(0) = 10^6$ and $\eta = 1$, subject to inverse Compton drag from the companion star photons, for PSR B1259-63 (a) and PSR J0045-73 (b). The pulsar-companion star separation is that at periastron. The curves correspond to different values of θ_p (see Fig. 1) as labelled.

scatterings stop the electrons in the wind of PSR J0045-73 at $\hat{r} \approx 0.7$, compared to the simple estimate $r_{\text{decel}} \sim 0.02D_\tau$. These differences arise primarily because the simple estimates ignored the Klein-Nishina effects — which reduce the scattering cross section from the Thompson value. The increasing density of target photons encountered by the wind electrons as they approach the companion star offsets the Klein-Nishina correction to some degree, but the net effect is that the deceleration length is much larger than suggested by the simple estimate.

Equation (7) can also be used to determine the position of the surface at which the radial wind loses a given fraction of its energy as a result of inverse Compton scattering. Such a surface is rotationally symmetric about the line joining the two stars. Cross sections of the surfaces where $\gamma_w(\hat{r})$ has fallen to 90%, 75% and 50% of its initial value are shown in Fig. 3 for PSR B1259-63 and PSR J0045-73 at periastron, for three different values of the initial Lorentz factor $\gamma_w(0)$. Unless the interaction between the stellar wind and the pulsar wind intervenes, we expect the pulsar wind to terminate roughly at the position where the wind electrons have lost half of their initial energy.

The shapes of the cross-sections in all the panels of Fig. 3 clearly show the strong dependence of the wind deceleration on the angle θ_p . The surfaces of equal loss are all closest to the pulsar along the line joining the pulsar to the Be star, and rapidly become more distant from the pulsar as θ_p increases. This occurs because while head-on collisions are effective at decelerating the electrons, the deceleration drops off very rapidly as θ_p increases, and the photon density also drops off very rapidly with distance from the pulsar at even moderate values of θ_p .

The dependence on $\gamma_w(0)$ as depicted in Fig. 3 is particularly striking. The

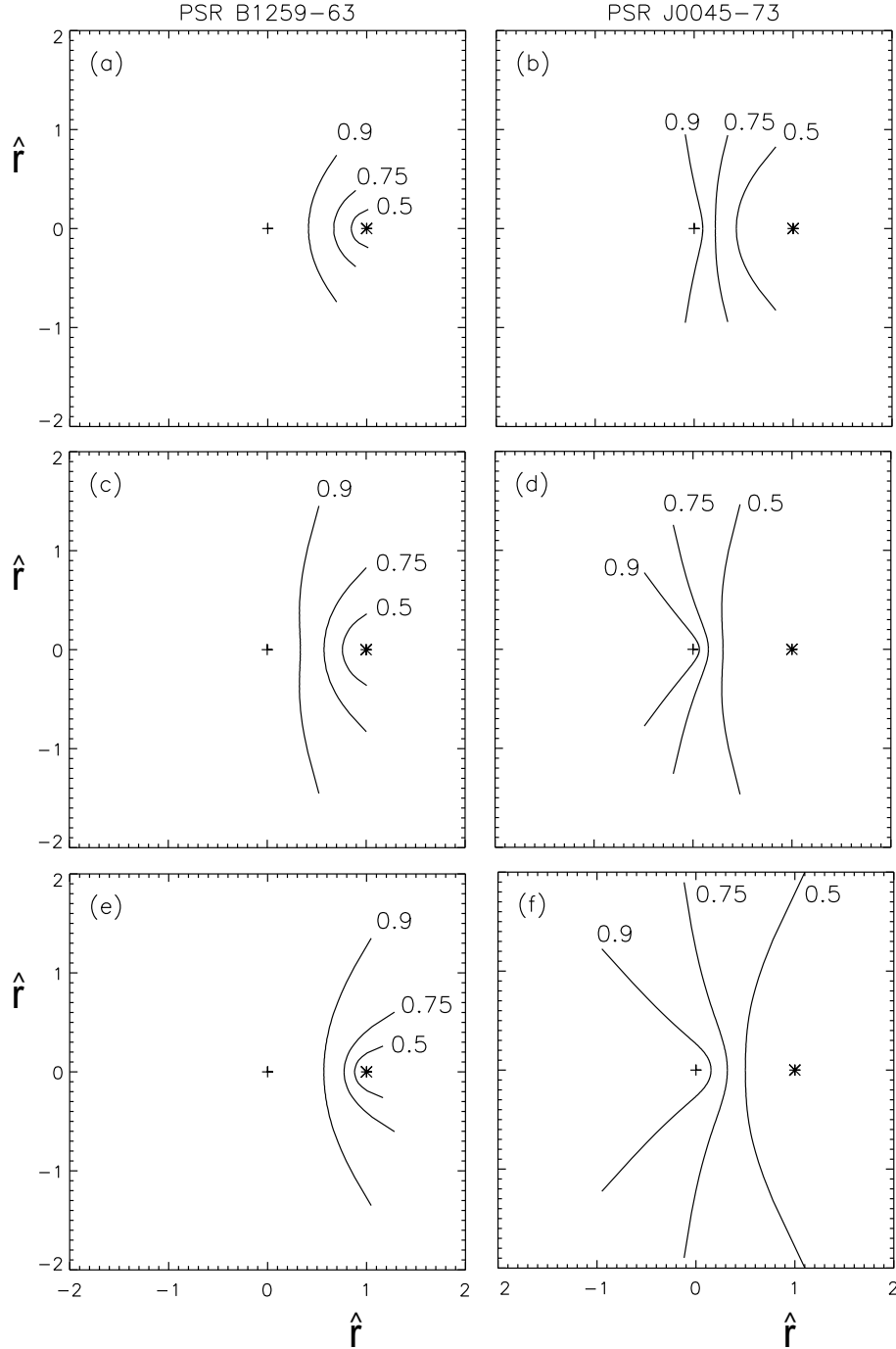


Fig. 3. Cross sections through the surfaces where $\gamma(\hat{r})$ has dropped to 90%, 75% and 50% of the initial value $\gamma_w(0)$ – as labelled, if inverse Compton drag is the dominant wind deceleration mechanism. The wind, orbit and target photon parameters are as for PSR B1259–63 (left) and for PSR J0045–73 (right) at periastron and are given in Table 1. The pulsar is at the origin and is marked by a plus and the companion star is marked by an asterisk. The two top panels (a) & (b) show the results when $\gamma_w(0) = 10^4$, the middle two (c) & (d) are for $\gamma_w(0) = 10^5$, and the lower two panels (e) & (f) are calculated for $\gamma_w(0) = 10^6$.

surfaces of equal loss are much closer to the pulsar, for both PSR B1259–63 and PSR J0045–73, when $\gamma_w(0) = 10^5$ than for either $\gamma_w(0) = 10^4$ or $\gamma_w(0) = 10^6$. This is an indication that the deceleration is most effective when the system is ‘tuned’ such that $\gamma\epsilon_0 \sim 1$. This occurs because the energy loss rate is made up of two parts, the scattering rate and the average energy loss per collision. The former is constant in the Thomson regime, but falls off with increasing energy in the Klein-Nishina regime. The average energy loss per collision divided by the energy of the scattering particle increases proportional to γ in the Thomson regime, and tends to a constant in the Klein-Nishina regime. The combined result of these effects is that there is a peak in the energy loss rate near the transition between the Thomson and Klein-Nishina regimes.

Finally, Fig. 3 shows the difference between the inverse Compton deceleration the winds of PSR B1259–63 and of PSR J0045–73. In PSR B1259–63 the density of photons from the companion star is not large enough to substantially decelerate the pulsar wind before it has travelled a substantial fraction of D_τ , even along the line joining the stars where the collisions are precisely head on. The surfaces depicted, which all have their apexes at $\hat{r} \gtrsim 0.25$, therefore wrap around the Be star rather than the pulsar. These results suggest that in PSR B1259–63 the inverse Compton drag is unlikely to terminate the pulsar wind before it attains pressure balance with the Be star outflow, given that this balance is expected to occur at $\hat{r} \lesssim 0.5$ [Melatos et al. 1995]. It is therefore reasonable to assume, with Kirk et al. [1999], that a termination shock forms in the pulsar wind as a result of pressure balance with the Be-star outflow. Nevertheless, in the case of PSR B1259–63 the conversion of even a small fraction of the wind energy could result in an observable flux. From Fig. 3 it is clear that if the wind terminates at a radius \hat{r}_T which is a significant fraction of the binary separation, it may become observable. For $\gamma_w(0) \sim 10^5$ and $\hat{r}_T \sim 0.5$ the figure indicates that at periastron the unshocked wind will lose approximately 25% of its momentum due to inverse Compton scattering along the line joining the stars, resulting in a substantial gamma-ray luminosity.

For PSR J0045–73 the situation is even more extreme. The companion star photon density at the pulsar is so large at periastron – because the orbital separation is so small – that inverse Compton drag is much more effective at decelerating the pulsar wind. In this system many of the surfaces of equal loss depicted have their apex very close to the pulsar and therefore wrap around the pulsar rather than the companion star. It is possible that inverse Compton drag may stop the wind of PSR J0045–73 before it attains pressure balance with the companion star outflow, at least at angles close to the line connecting the stars, and at times close to periastron.

5 Emitted gamma rays

5.1 Spectra

This section details the spectrum of inverse Compton emission produced via scattering from the unshocked wind. We assume that the wind momentum is carried entirely by electrons and positrons ($\eta = 1$), that the only deceleration is that from the scattering, and that the wind expands freely without being terminated via pressure balance with the companion star outflow ($\hat{r}_T \gg 1$). The spectra obtained by integrating equations (7) and (18) with (19), for a range of wind Lorentz factors $\gamma_w(0)$ and at three different angles θ_p with other parameters relevant to PSR B1259–63 at periastron, are presented in Fig. 4. Note that the spectra show the energy flux versus the photon energy. The emitted spectra depend dramatically on both the angle θ_p and on $\gamma_w(0)$.

For $\theta_p = 5^\circ$ (a value not, however, observable from the Earth) the wind electrons are initially directed almost along the line connecting the pulsar and its companion. Inverse Compton scattering is thus intrinsically efficient as the electron-photon collisions are close to head on, and the electrons in the wind encounter a very large target photon density as they pass close to the companion star. Integration over the scatterings occurring along such a radius therefore produces a relatively broad spectrum of emitted photons because of the wide range of Lorentz factors of the scattering electrons. Furthermore, the scattered emission is relatively bright because the wind loses a substantial fraction of its momentum to the scattered photons.

For $\theta_p = 125^\circ$ the wind electrons are initially directed more or less away from the companion star, so the scatterings are very far from head on and the target photon density decreases very rapidly as the electrons propagate away from the pulsar (and hence from the companion star). The emitted spectrum in this case is close to monochromatic because the electron deceleration is very small so the scattering particles are essentially monoenergetic. Furthermore, since only a small fraction of the wind momentum is transferred to the scattered photons, the flux of the scattered photons is commensurately small.

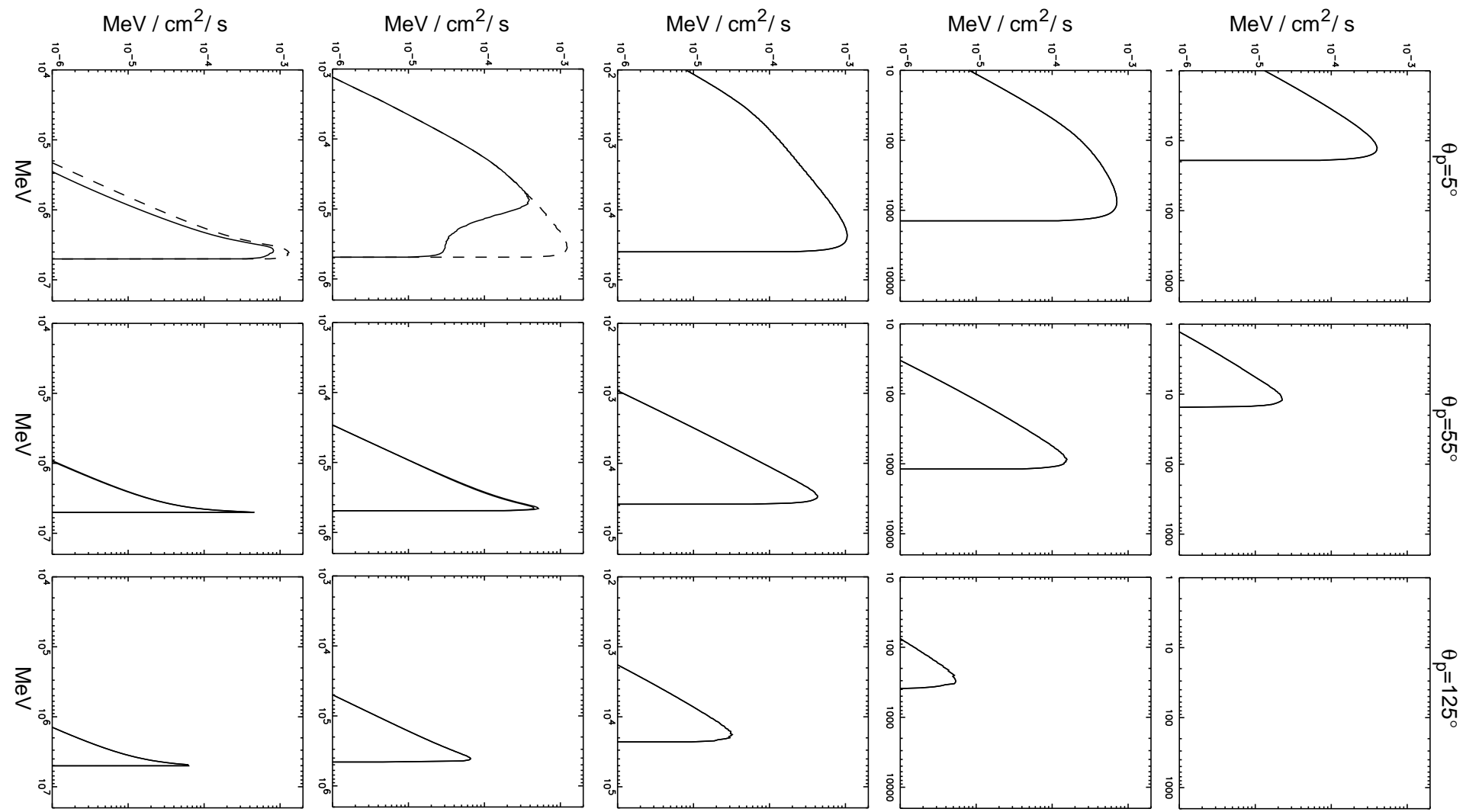


Fig. 4. The SED (spectral energy distribution) EF_E with F_E the energy flux at the distance of the Earth of inverse Compton scattered photons as a function of photon energy – at angles $\theta_p = 5^\circ$ (left), 65° (middle), and 125° (right). The top row of spectra are calculated for a pulsar wind with an initial Lorentz factor $\gamma_w(0) = 10^3$. Each subsequent set of three spectra down the page has $\gamma_w(0)$ increased by a factor of 10, so that the bottom row represents the emission for $\gamma_w(0) = 10^7$. The other parameters are the same for all panels, and are appropriate for PSR B1259–63 at periastron. The dashed curves show the spectra calculated by ignoring the absorption due to pair production, i.e. by artificially setting $d\tau/d\hat{r} = 0$ in Eq. (18). The solid curves include the effects of the pair production optical depth. Note that the energy scales are the same for each set of three spectra for a given wind Lorentz factor, but the scale shifts up a decade with each factor of ten increase in $\gamma_w(0)$. The energy flux scales are the same for all panels.

The dependence of the emitted spectra on $\gamma_w(0)$ is also striking. The energy of the scattered photons increases strongly as the wind Lorentz factor increases; e.g. for $\gamma_w(0) = 10^3$ the peak of the emitted spectrum occurs just above 10 MeV while for $\gamma_w(0) = 10^4$ the peak is at ≈ 1000 MeV. The energy of the scattered photons therefore scales as $\sim \gamma^2$ in this regime, as expected since for these Lorentz factors $\gamma\epsilon_0 \ll 1$ and the scattering is in the Thompson regime. As the wind Lorentz factor is increased further the peak of the spectrum of scattered photons continues to move up in energy, but the increase is slower than γ^2 due to the increasing importance of the Klein-Nishina effects. The broadening of the spectrum as $\gamma_w(0)$ increases to around 10^5 and the subsequent narrowing as γ increases further is dramatically illustrated by the left-hand panels for $\theta_p = 5^\circ$. This is another example of the effects of tuning the system to maximize the scattering efficiency, resulting in the greatest deceleration and correspondingly broad energy distribution of the scattering particles, at $\gamma\epsilon_0 \sim 1$.

The shape of each individual spectrum is also indicative of the degree of deceleration effected by the scattering. All the spectra cut off abruptly at high energies reflecting the maximum energy ϵ_{out}^+ of the scattered photons. The spectrum calculated for $\gamma_w = 10^5$ and $\theta_p = 5^\circ$ rises relatively steeply at the lowest energies shown, then turns over and rises more slowly for about 1.5 decades in energy (above 10^3 MeV) before dropping steeply towards the upper cutoff. The steeply-rising portion of the spectrum at low energies is increasing as $\epsilon_{\text{out}}^{1/2}$ corresponding to a flux density which decreases as $\epsilon_{\text{out}}^{-1/2}$ – the usual spectrum for inverse Compton emission from a single electron in the classical Thompson regime. This portion of the emitted spectrum is dominated by the electrons at the minimum Lorentz factor attained after deceleration of the wind. The flatter portion of the spectrum corresponds to the emission from the decelerating portion of the wind — integrated over a relatively broad range of γ_w ; it is only evident when both $\gamma_w(0)$ and θ_p have values which lead to a substantial deceleration. When this is not the case the spectra take one of two forms: if $\gamma\epsilon_0 \ll 1$ the SED increases as $\epsilon_{\text{out}}^{1/2}$ right up to the cutoff at ϵ_{out}^+ ; if $\gamma\epsilon_0 \gtrsim 1$ the Klein-Nishina effects are important and the SED rises much more

steeply to a peak near ϵ_{out}^+ and the emission is essentially monochromatic.

Finally, Fig. 4 shows the effects of absorption due to pair production. For $\gamma_w(0) \lesssim 10^5$ the scattered photons are below the threshold energy required for pair production on the target photons even when θ_p is small, and so there is no absorption. The absorption due to pair production is most significant in the spectrum plotted for $\gamma_w(0) = 10^6$ and $\theta_p = 5^\circ$ where it removes a substantial part of the emission at energies up to a decade below the peak. For smaller γ_w the scattered photons are below the threshold for absorption, whereas at higher values the resonant character of the cross section becomes apparent.

5.2 Light curves

The inclination angle of the orbit of PSR B1259–63 is $i = 35^\circ$ so a telescope on the Earth will sample angles θ_p between $90 - i = 55^\circ$ and $90 + i = 125^\circ$ over the binary period. These extremes are the two larger values of θ_p for which the spectra are plotted in Fig. 4. The increase from the minimum value of θ_p to the maximum occurs over just 65 days beginning on day -6 , just before periastron. The subsequent decrease occurs far more slowly over the remaining 1170 days of the orbital period. This variation, together with the variation in the target photon density due to the changing binary separation during the orbit, results in a profound variation in the emission of inverse Compton scattered radiation from the binary system.

Fig. 5 shows the orbital variation of the integrated flux density, $\int F_E dE$, expected from PSR B1259–63 for $\gamma_w(0) = 10^4$, 10^5 and 10^7 . The light curve for $\gamma_w(0) = 10^6$ is very similar to that for $\gamma_w(0) = 10^5$ so it has been omitted for clarity. The total variation in the integrated flux is very large; for $\gamma_w = 10^4$ the peak is two orders of magnitude above the minimum. The light curves are also very strongly peaked and clearly asymmetric, with the increase towards the maximum integrated flux occurring somewhat more gradually than the decline to the minimum. The asymmetry, peak to minimum ratio, and peaked nature of the light curves are minimized when $\gamma_w(0)\epsilon_0 \sim 1$, but even then the peak to minimum ratio is more than a factor of ten. These features are all a direct reflection of the orbital variation of the binary separation and the angle θ_p ; the asymmetry is a straightforward manifestation of the asymmetry in the variation of θ_p about periastron.

The peak of the spectrum of the scattered photons also varies with orbital phase. If this variation were to cross the threshold of an observing instrument the detected light curve could be somewhat different from those shown in Fig. 5. The energy spectra at the extreme values of θ_p sampled during one binary orbit are shown in the second and third columns of Fig. 4. The variation

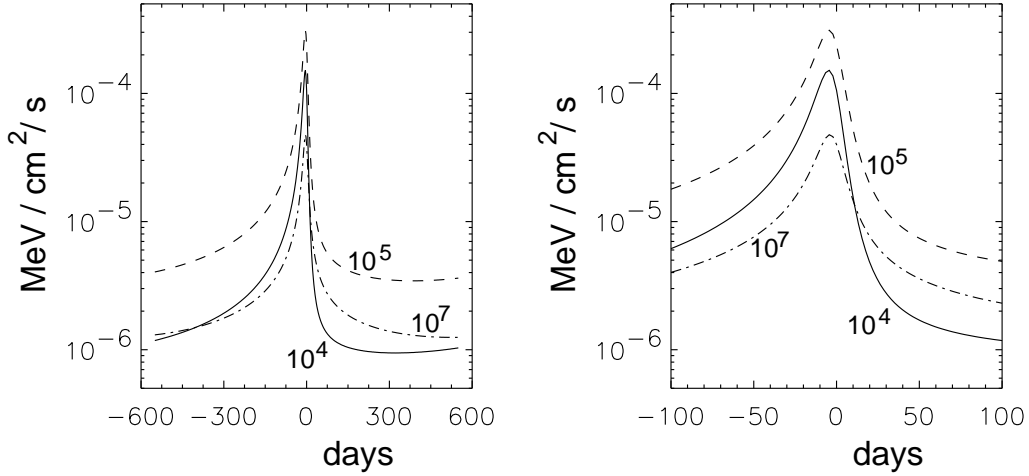


Fig. 5. Light curves showing the integrated energy flux at the Earth from PSR B1259–63. The different curves correspond to different initial wind speeds: the solid curve is for $\gamma_w(0) = 10^4$, the dashed curve is for $\gamma_w(0) = 10^5$, and the dot-dashed curve is for $\gamma_w(0) = 10^7$. The left panel shows the variation over the entire orbit and the right panel shows just 200 days centered on periastron.

in the peak energy is largest when $\gamma_w(0)\epsilon_0 \lesssim 1$. For $\gamma_w(0) = 10^4$ the peak is at ~ 1000 MeV just prior to periastron (when θ_p attains its minimum value), and it moves down to ~ 200 MeV by about day +60 (corresponding to the maximum of θ_p). For $\gamma_w(0) = 10^5$ the peak moves from ~ 30 GeV to ~ 20 GeV, while for $\gamma_w(0) = 10^6$ and $\gamma_w(0) = 10^7$ the peak is at ~ 300 GeV and ~ 5 TeV respectively, and moves very little.

The integrated flux shown in Fig. 5 does not include the effects of absorption due to pair production. Calculations including the pair production optical depth indicate that its effect on the integrated flux density from PSR B1259–63 is small – reducing the integrated flux density by $\sim 10\%$ or less – and that the reduction is relatively insensitive to the orbital phase. It is therefore unimportant for observations of the inverse Compton emission.

6 Discussion

The models for the inverse Compton emission from the freely-expanding wind of PSR B1259–63 presented in §5 suggest that the emission is likely to be detectable at energies somewhere in the GeV to TeV range, depending on the wind parameters. Given the present lack of operational γ -ray telescopes, the best opportunity for detecting the emission is in the TeV energy range.

In calculating the inverse Compton emission spectra we optimistically assume that none of the wind momentum is carried by ions and that the wind is not terminated via pressure balance with the companion star outflow. The results indicate that if the initial Lorentz factor of the wind is in the range 10^6 – 10^7 the inverse Compton emission from the unshocked wind at epochs near periastron could be as much as a factor of 100–1000 above the sensitivity threshold of the new CANGAROO II imaging Cerenkov detector [Yoshikoshi et al. 1999] which should be operational before the end of 1999. If the pulsar wind is slower, the inverse Compton emission should be detectable by the GLAST observatory at energies in the range 20 MeV–300 GeV if $\gamma_w(0) \sim 10^4 - 10^5$, or by the INTEGRAL project at energies up to 10 MeV if $\gamma_w(0) \sim 10^3$. The sensitivity of each of these planned satellite-borne observatories is easily sufficient to detect the model emission. However, they will not operate until well after the next periastron.

If either of the fundamental assumptions regarding the pulsar wind is not applicable to the PSR B1259–63 system, the gamma-ray emission from the unshocked wind will be lower than suggested by the models detailed in §5. If the momentum flux of the pulsar wind is sufficiently small that it is dominated by the Be-star outflow, then the pulsar wind will terminate close to the pulsar at a shock which is wrapped around the pulsar. The mismatch between the shape of this termination shock and the loss surfaces due to inverse Compton scattering could then lead to integrated-flux light curves that are quite different to those presented in Fig. 5. Furthermore, the inverse Compton deceleration of the pulsar wind decreases its ram pressure, reducing the termination shock radius, but this effect will be small at values of θ_p which can be observed. The nature of the gamma-ray light curves will depend on both the stand-off distance and the details of the shape and orientation of the pulsar wind termination shock.

Observations of changes in the pulsed emission from PSR B1259–63 [Johnston et al. 1996] and observations and interpretation of the unpulsed radio emission seen around periastron [Johnston et al. 1999; Ball et al. 1999] indicate that the pulsar and its wind interact with a disk surrounding the Be star between about day -25 and $+25$. There are few observations of X-ray and γ -ray emission from this system at epochs outside this range. Tavani & Arons

[1997] have addressed the problem of fitting the X-ray observations close to periastron with the inverse Compton emission from the shocked pulsar wind. Their analysis indicates that the details of the flow pattern, the competition between adiabatic and radiative losses, and strong shielding (or shadowing) of the target photons by the pulsar disk, are all important near the epoch of periastron. These details are not considered in our work here, and the light curves of Fig. 5 can therefore not be expected to be accurate at epochs close to periastron. Nevertheless the upper limits from EGRET measurements [Tavani et al. 1996] just prior to the 1994 periastron place some constraint on the pulsar wind parameters. In particular, the inverse Compton spectrum from an unbounded lepton wind with an initial Lorentz factor of $\gamma_w(0) = 10^4$ (as shown in Fig. 4) would exceed the EGRET upper limits which imply that the energy flux of photons at energies of 30 MeV to 10 GeV is less than about $2 \times 10^{-5} \text{ MeV cm}^{-2} \text{ s}^{-1}$.

The periastron to apastron ratio of inverse Compton emission from an unbounded lepton wind from PSR B1259–63 as shown in Fig. 5 is much larger than the flux ratio from the shock-accelerated electrons when the wind terminates close to the pulsar [Kirk et al. 1999]. Observations of the high-energy light curve may therefore enable the deconvolution of the two contributions to the γ -ray emission. In particular, observations aimed at detecting an asymmetric light curve at energies in the MeV–TeV range, or at least placing firm upper limits on the high energy emission from this system, should provide valuable information on the properties of the unshocked pulsar wind.

Acknowledgements

We thank Simon Johnston for many helpful discussions, and LTB thanks Olaf Skjæraasen for assistance with Fig. 3. Our collaboration was made possible by support for JGK by the RCfTA under its International Visitor program, and for LTB from the MPIK Heidelberg.

Appendix A: Energy and momentum balance

Assuming the magnetic field to be weak, the equations of conservation of energy and radial momentum flux in the wind take on the forms:

$$\frac{1}{r^2} \frac{d}{dr} \left[r^2 (E + P) \beta_w \gamma_w^2 \right] = C^0 \equiv n_e \left\langle \frac{1}{c} \frac{de}{d\tau} \right\rangle \quad (20)$$

$$\frac{1}{r^2} \frac{d}{dr} \left\{ r^2 \left[(E + P) \beta_w^2 \gamma_w^2 + P \right] \right\} = C^r \equiv n_e \left\langle \frac{dp_r}{d\tau} \right\rangle \quad (21)$$

[e.g., Landau & Lifshitz 1959] Here, E and P denote the proper gas energy density (including rest-mass) and pressure, respectively. The radial velocity of the gas is $c\beta_w$ and the associated Lorentz factor is γ_w . The components C^0 and C^r of the four-force density on the right-hand sides of Eqs. (20) and (21) are proportional to the proper number density n_e of electrons and positrons taken together and to the average rates of energy and radial momentum change of a single electron due to Compton scattering: $\langle de/d\tau \rangle$ and $\langle dp_r/d\tau \rangle$ where τ is the proper time, measured in the rest frame of the wind.

The average rate of change of energy of the photon field is given by an integral similar to that in equation (1) with the additional weight factor $\epsilon_{\text{out}} - \epsilon_{\text{in}}$. Equating the energy loss rate by the electron to the gain by the photon field leads, after a straightforward calculation, to the expression

$$\left\langle \frac{1}{c} \frac{de}{dt} \right\rangle = -\frac{3}{8} \sigma_T m_e c^2 \int d\vec{\Omega} d\epsilon_{\text{in}} \frac{\epsilon_{\text{in}}'^2}{\epsilon_{\text{in}}} \left(1 - \frac{\epsilon_{\text{in}}}{\gamma \epsilon_{\text{in}}'} - \frac{\epsilon_{\text{in}}}{\gamma} \right) \times n_\gamma(\epsilon_{\text{in}}, \mathbf{R}, \vec{\Omega}) F_{\text{loss}}(\epsilon_{\text{in}}'). \quad (22)$$

The rate of change of radial momentum is calculated in a similar fashion, using the quantity $-\epsilon_{\text{out}} \cos \theta_{\text{out}} + \epsilon_{\text{in}} \cos \theta_{\text{in}}$ as the weighting function, which gives

$$\left\langle \frac{dp_r}{dt} \right\rangle = -\frac{3}{8\beta} \sigma_T m_e c \int d\vec{\Omega} d\epsilon_{\text{in}} \frac{\epsilon_{\text{in}}'^2}{\epsilon_{\text{in}}} \left(1 - \frac{\epsilon_{\text{in}}}{\gamma \epsilon_{\text{in}}'} - \frac{\epsilon_{\text{in}}}{\gamma} + \frac{\epsilon_{\text{in}}'}{\gamma^2} \right) \times n_\gamma(\epsilon_{\text{in}}, \mathbf{R}, \vec{\Omega}) F_{\text{loss}}(\epsilon_{\text{in}}'). \quad (23)$$

The amount of heating is given by the projection of the four-force density onto the velocity. Inspection of Eqs. (22) and (23) reveals that only the fourth term $\epsilon_{\text{in}}'/\gamma^2$ in parentheses in Eq. (23) survives the projection. In the case of an ultra-relativistic wind this term is small ($\sim \epsilon_{\text{in}}/\gamma$) compared to the leading ones in the expression for the work done decelerating the electron, and we neglect it in the following. In this approximation, we set $P = 0$ and $E/c^2 = \rho_w$, the proper rest-mass density, and identify the Lorentz factor of the

wind with that of each individual electron. As a result, one of the equations (20) and (21) is superfluous. Keeping the energy equation (20), and combining it with the equation of mass conservation, which reads

$$\frac{1}{r^2} \frac{d}{dr} \left(r^2 \rho_w \beta_w \gamma_w \right) = 0 \quad (24)$$

one finds

$$\begin{aligned} \frac{d\gamma_w}{dr} &= \frac{\eta}{m_e c^3 \beta_w \gamma_w} \left\langle \frac{de}{d\tau} \right\rangle \\ &= \frac{\eta}{m_e c^3 \beta_w} \left\langle \frac{de}{dt} \right\rangle. \end{aligned} \quad (25)$$

Equation (3) follows directly through substitution of (22) into (25).

Appendix B: Radiation transfer of inverse Compton emission

The differential number density of electrons in the pulsar wind follows directly from equation (15) and is given by

$$\begin{aligned} \frac{dN_e}{d\gamma d\vec{\Omega} dr} &= r^2 N_e(r) \delta[\gamma - \gamma_w(r)] \\ &\approx \frac{\eta L_w}{4\pi \gamma_w(0) m_e c^3} \delta[\gamma - \gamma_w(r)] \end{aligned} \quad (26)$$

where we have assumed $\beta_w \approx 1$.

The radiative transport equation governing the specific intensity $I(\epsilon_{\text{out}}, r)$, including both emission by inverse Compton scattering and absorption by photon-photon pair production, is

$$\frac{dI}{dr} = \epsilon_{\text{out}} m_e c^2 \eta_{\text{ic}} + I \frac{d\tau}{dr}. \quad (27)$$

The quantity η_{ic} is the inverse Compton emissivity, the number of photons emitted per second per unit volume per unit energy interval around $\epsilon_{\text{out}} m_e c^2$, which is given by

$$\begin{aligned} \eta_{\text{ic}} &= \frac{1}{m_e c^2} \int d\gamma \frac{dN_e}{d\gamma d\vec{\Omega} dr} \frac{dN_\gamma}{d\epsilon_{\text{out}} dt} \\ &= \left(\frac{L_w}{4\pi} \right) \frac{\eta}{\gamma_w(0) (m_e c^2)^2 c} \frac{dN_\gamma}{d\epsilon_{\text{out}} dt} \end{aligned} \quad (28)$$

where $dN_\gamma/d\epsilon_{\text{out}} dt$ is the differential rate of emission of photons by a single electron.

The function $\mathcal{H}(\epsilon_{\text{out}}, \cos \psi)$ which appears in the photon production rate, Eq. (17), is related to the quantity $dN_\gamma/dtd\epsilon_{\text{out}}[d\epsilon_{\text{in}} dx']$ derived by Ho & Epstein [1989, Eq. A14], and is defined by

$$\begin{aligned} \mathcal{H}(\epsilon_{\text{out}}, \cos \psi) &= \frac{3\xi}{8\gamma^2 \epsilon_{\text{in}}} \frac{1}{[(1 - \lambda - \xi)^2 + \beta^2(1 - x'^2)]^{1/2}} \times \\ &\quad \left[\frac{1}{\xi} + \frac{y_0^2}{(a^2 - b^2)^{1/2}} + \left(\frac{2y_0}{\epsilon} + \frac{a}{\epsilon^2} \right) + \right. \\ &\quad \left. \left(\frac{a}{(a^2 - b^2)^{1/2}} - 1 \right) + \frac{a\xi - a^2 + b^2}{(a^2 - b^2)^{3/2}} \right] \end{aligned} \quad (29)$$

with

$$\xi = 1 - \beta_w x', \quad \lambda = \epsilon_{\text{out}}/\gamma_w, \quad \epsilon = \epsilon_{\text{in}}/\gamma_w, \quad (30)$$

$$x' = \frac{\beta_w - \cos \psi}{1 - \beta_w \cos \psi} \quad (31)$$

and where

$$a = \xi + \varepsilon(1 - y_0), \quad b = -\varepsilon\delta \quad (32)$$

$$y_0 = \frac{(1 - \lambda - \xi)(1 - \lambda - \rho\xi)}{(1 - \lambda - \xi)^2 + \beta^2(1 - x'^2)}, \quad (33)$$

$$\delta = \frac{\beta(1 - x'^2)^{1/2}[\beta^2 + 2\lambda(1 - \rho)\xi - (1 - \rho\xi)^2]^{1/2}}{(1 - \lambda - \xi)^2 + \beta^2(1 - x'^2)}, \quad (34)$$

and finally

$$\rho = \frac{\epsilon_{\text{out}}}{\epsilon_{\text{in}}}. \quad (35)$$

However, this function gives the photon production rate only when $\epsilon_{\text{out}}^- \leq \epsilon_{\text{out}} \leq \epsilon_{\text{out}}^+$ where

$$\epsilon_{\text{out}}^- = \frac{\gamma\varepsilon(1 - \beta \cos \psi)}{(1 + \varepsilon + Q_\varepsilon)}, \quad \text{and} \quad \epsilon_{\text{out}}^+ = \frac{\gamma\varepsilon(1 + \varepsilon + Q_\varepsilon)}{(\xi + 2\varepsilon)} \quad (36)$$

with

$$Q_\varepsilon = (\beta^2 + \varepsilon^2 + 2\beta\varepsilon \cos \psi). \quad (37)$$

At these limits the term $[\beta^2 + 2\lambda(1 - \rho)\xi - (1 - \rho\xi)^2]^{1/2}$ in the quantity δ becomes zero, and outside this range the photon production rate is zero.

The differential optical depth due to pair production was given by Kirk et al. [1999, Eq. B4] In our notation it is

$$\hat{\sigma}_{\gamma\gamma}(x) = \begin{cases} \frac{3}{16}(1 - \zeta^2) \left[(3 - \zeta^4) \ln \left(\frac{1+\zeta}{1-\zeta} \right) - 2\zeta(2 - \zeta^2) \right] & \text{if } x \geq 1 \\ 0 & \text{otherwise} \end{cases} \quad (38)$$

where

$$\zeta = \frac{(x^2 - 1)^{1/2}}{x}. \quad (39)$$

References

- [1] Aharonian, F. A., Bogovalov, S. V., 1999, *Astron. Nach.*, in press
- [2] Aschenbach, B., Brinkmann, W., 1975, *A&A*, 41, 147
- [3] Ball, L., Melatos, A. M., Johnston, S., Skjæraasen, O., 1999, *ApJ*, 541, L39
- [4] Bell, J. F., Bessell, M. S., Stappers, B. W., Bailes, M., Kaspi, V. M., 1995, *ApJ*, 447, L117
- [5] Bogovalov, S. V., Aharonian, F. A., 1999, *MNRAS*, submitted
- [6] Chernyakova, M. A., Illarionov, A. F., 1999, *MNRAS*, 304, 359
- [7] De Jager, O. C., Harding, A. K., 1992, *ApJ*, 396, 161
- [8] Emmering R. T., Chevalier R. A., 1987, *ApJ*, 321, 334
- [9] Harding, A. K., 1996, *Space Sc. Rev.*, 75, 257
- [10] Hester, J. J., 1995, *ApJ*, 448, 240
- [11] Hirayama, M., Nagase, F., Tavani, M., Kaspi, V. M., Kawai, N., Arons, J., 1996, *PASJ*, 48, 833
- [12] Ho, C., Epstein, R. I., 1989, *ApJ*, 343, 277
- [13] Johnston, S., Manchester, R. N., Lyne, A. G., Bailes, M., Kaspi, V. M., Qiao, G., D'Amico, N., 1992, *ApJ*, 387, L37
- [14] Johnston, S., Manchester, R. N., Lyne, A. G., Nicastro, L., Spyromilio, J., 1994, *MNRAS*, 268, 430
- [15] Johnston, S., Manchester, R. N., Lyne, A. G., D'Amico, N., Bailes, M., Gaensler, B. M., Nicastro, L., 1996, *MNRAS*, 279, 1026
- [16] Johnston, S., Manchester, R. N., McConnell, D., Campbell-Wilson, D., 1999, *MNRAS*, 302, 277
- [17] Jones, F. C., 1965, *Phys. Rev. B*, 137, 1306
- [18] Kaspi, V. M., Johnston, S., Bell, J. F., Manchester, R. N., Bailes, M., Bessell, M., Lyne, A. G., D'Amico, N., 1994a, *ApJ*, 423, L43
- [19] Kaspi, V. M., Bell, J. F., Bessell, M., Stappers, B., Bailes, M., Manchester, R. N., 1994b, *AAS*, 185, 6207
- [20] Kennel, C. F., Coroniti, F. V., 1984, *ApJ*, 283, 710
- [21] Kirk, J. G., Ball, L., Skjæraasen, O., 1999, *Astroparticle Phys.*, 10, 31
- [22] Landau, L. D., Lifshitz, E. M., 1959, *Fluid Dynamics*, Pergamon press: Oxford
- [23] Mastichiadis, A., 1991, *MNRAS*, 253, 235

- [24] Melatos, A., Johnston, S., Melrose, D. B., 1995, MNRAS, 275, 381
- [25] Qiao, G. J., Lin, W. P., 1998, A&A, 333,172
- [26] Luo, Q., Protheroe, R. J., 1998, Publ. Astron. Soc. Aust., 15, 222
- [27] Rees, M. J., Gunn, J. E., 1974, MNRAS, 167, 1
- [28] Sako, T., et al., 1997, Proc. 25th ICRC (Durban), 3, 165
- [29] Tavani, M., et al., 1996, A&AS, 120, 221
- [30] Tavani, M., Arons, J., 1997, ApJ, 477, 439
- [31] Underhill, A., Doazan, V., 1982, 'B stars with and without emission lines',
NASA SP-456
- [32] Yoshikoshi, T., et al., 1999, Astroparticle Phys., 11, 267
- [33] Zhang, B., Qiao, G. J., Han, J. L., 1997, ApJ, 491, 891